



Heteroatoms binary-doped hierarchical porous g-C₃N₄ nanobelts for remarkably enhanced visible-light-driven hydrogen evolution

Jiaojiao Wu^a, Nan Li^a, Xiao-Hong Zhang^a, Hua-Bin Fang^a, Yan-Zhen Zheng^b, Xia Tao^{a,b,*}

^a State Key Laboratory of Organic-Inorganic Composites, Beijing University of Chemical Technology, Beijing 100029, China

^b Research Center of the Ministry of Education for High Gravity Engineering & Technology, Beijing University of Chemical Technology, Beijing 100029, China

ARTICLE INFO

Keywords:

g-C₃N₄ photocatalyst
C, O co-doping
Hierarchical porous nanobelt
Visible photocatalytic H₂ evolution

ABSTRACT

The heteroatoms C, O binary-doped g-C₃N₄ (C-O/CN) with hierarchical porous nanobelt architecture was synthesized via a straightforward template-free self-assembly method using dicyandiamide as g-C₃N₄ precursor and glutathione as C, O doping source. The as-prepared C-O/CN exhibits well-defined hierarchical nanobelt structure composed of porous nanosheets, resulting in obvious enhanced specific surface area (120 m² g⁻¹). Particularly, C, O heteroatoms, introduced into the structure of g-C₃N₄ by substituting N atoms, induce narrowed bandgap for more effective visible-light harvesting and negatively shifted conduction band position for stronger reducibility of electrons for H₂ production. Such hierarchical porous C-O/CN nanobelts are demonstrated to be highly efficient in charge separation and transfer. Under optimal mass ratio of glutathione to dicyandiamide (0.1%), C-O/CN-0.1 shows a highest H₂ evolution rate of 18.38 mmol h⁻¹ g⁻¹ under visible-light ($\lambda > 420$ nm) irradiation (about 79.9 times higher than that of the bulk g-C₃N₄) and a remarkable apparent quantum efficiency of 9.83% at 420 nm, which can be used as a promising low-cost photocatalyst for H₂ evolution.

1. Introduction

Metal-free graphitic carbon nitride (g-C₃N₄) plays an increasingly significant role in visible-light photocatalytic solar-to-H₂ conversion system due to its electronic-band structure tenability, thermal/chemical stability and low cost with earth-abundance carbon and nitrogen, which, however, also faces the invalidation in virtue of its intrinsic drawbacks such as poor surface area, unsatisfactory visible-light harvesting and rapid recombination of photo-excited charge transfer [1–5]. As a consequence, the photocatalytic activity of the bulk g-C₃N₄ is still not high enough for practical application. Various strategies have been developing to address these issues, for instance, coupling with other narrow bandgap semiconductors, integration with conductive materials or co-catalysts, construction of various nanoarchitectures and introduction of heteroatoms [6–9].

Non-metal heteroatom (B, C, N, O, S, P and I) [10–16] doping is an effective strategy to elevate the visible-light-driven catalytic activity of g-C₃N₄. Studies conducted on doping with C [11,17] (i.e. substituting N or directly inserting C) have recently attracted much attention in the g-C₃N₄ photocatalytic domain. Several investigations have demonstrated that C doping could form delocalized π -bonds among the substituted C and the hexatomic rings to modify electronic-band structure and charge transfer, resulting in enhancing utilization of visible-light and

photocatalytic abilities [11,17,18]. Apart from C doping, O doped g-C₃N₄ catalysts have recently shown promising photo-response and catalytic activity [13,19–22]. For examples, Huang et al. [13] reported a porous O doped g-C₃N₄ fabricated by a facile H₂O₂ thermal condensation method, and demonstrated that O doping could enhance the harvesting of visible-light and promote charge separation efficiency for H₂ evolution. Most recently, Ye and coworkers [22] reported a surface modification porous g-C₃N₄ by heating precursor at oxygen atmosphere. The thermally oxidized g-C₃N₄, in which trace amount of N in the –NH₂ terminals was replaced by O, displayed a significantly narrowed bandgap, negative shifted conduction band position and much higher photocatalytic H₂ evolution activity than that of the bulk g-C₃N₄. Clearly, C or O doping can improve photocatalytic H₂ evolution activity of g-C₃N₄ by modulating texture and intrinsic electronic-band structure, and further boosting light absorption range, reducibility of electrons for H₂ production and separation of photo-excited charge transfer. In fact, the simultaneous doping of two kinds of atoms into g-C₃N₄ such as P, S co-doping [23], P, C co-doping [24] and P, O co-doping [25] has been demonstrated to show higher photocatalytic activity and unusual physiochemical characteristics in comparison with single element doping. Therefore, developing C, O co-doped g-C₃N₄ materials with boosted photocatalytic activity is highly desirable, which has yet to be reported so far.

* Corresponding author at: State Key Laboratory of Organic-Inorganic Composites, Beijing University of Chemical Technology, Beijing 100029, China.
E-mail addresses: taoxia@mail.buct.edu.cn, taoxia@yahoo.com (X. Tao).

In addition to the heteroatom doping, rational design of g-C₃N₄ nanostructure is another viable strategy to enhance photocatalytic performance by enhancing specific surface area to expose more activity sites and strengthen mass transfer [26–29]. Hierarchical nanostructure, interconnecting the individual g-C₃N₄ nanosheets into another nanoarchitectures (e.g. nanotube and nanospheres) can effectively avoid the agglomeration of nanosheets in the bulk g-C₃N₄; simultaneously the multifaceted open-up nanosheets surface with sharp edges and abundant porous networks structure can achieve fast charge collection and separation, boosted light absorption, and rapid diffusion of reactants and products [19,30]. However, most reported non-metal heteroatom doped g-C₃N₄ materials did not possess hierarchical porous architecture [12,23,25] or hierarchical porous structures were obtained from exfoliating the bulk g-C₃N₄ by high-temperature oxidation process [19] or hazardous reagents [21].

In this context, the integration of the favorable features of foreign atoms C, O doping as well as hierarchical porous structure to fabricate a superior g-C₃N₄ based photocatalyst via a simple and environment-friendly methodology is urgent. Herein, we for the first time report heteroatoms C, O binary-doped g-C₃N₄ (denoted as C–O/CN) with hierarchical porous structure via a straightforward and eco-friendly template-free self-assembly method, in which glutathione (GLU), an oxygen-rich carbon material widely existed in human and animal cells, is chosen as the doping source of C and O. The resultant C–O/CN exhibits well-defined hierarchical nanobelt architecture composed of porous nanosheets, resulting in over 10-folds enhancement of specific surface area comparing with the bulk g-C₃N₄ (bulk-CN). Besides, we find that C and O doping by substituting trace amount of N in –NH_x groups and triazine rings respectively can optimize electronic-band structure for enhancing visible-light absorption and reducibility of electrons for H₂ production. Such hierarchical porous C–O/CN nanobelts are experimentally demonstrated to be more efficient in charge transfer and separation than bulk-CN. Consequently, the C–O/CN exhibits a dramatically enhanced H₂ evolution rate, climbing up to 18.38 mmol h^{−1} g^{−1} under visible-light ($\lambda > 420$ nm) irradiation, about 79.9 times than that of bulk-CN (0.23 mmol h^{−1} g^{−1}), which leads to a reasonably high apparent quantum efficiency (AQE) of 9.83% at 420 nm.

2. Experimental

2.1. Preparation of photocatalysts

The hierarchical porous C–O/CN nanobelts photocatalyst was synthesized as follows. First, dicyandiamide (DCDA) (3 g) and different ratios of glutathione (GLU) were added into deionized water (75 mL). Then, the mixture was placed into ultrasonic bath for 30 min to obtain homogeneous mixed solution. Third, the obtained solution was sealed in Teflon-lined autoclave and heated at 200 °C in a muffle furnace for 4 h. Afterwards, the resultant suspension solution (G-D solution) was kept in refrigerator 5 h and then freeze-dried to obtain G-D nanobelts. Note that the mass ratio of GLU to DCDA was chosen as 0%, 0.05%, 0.1%, 0.2% and 0.3%, denoted as G-D-0, G-D-0.05, G-D-0.1, G-D-0.2 and G-D-0.3, respectively. The final hierarchical porous C–O/CN nanobelts were collected by thermal treatment of G-D nanobelts at 520 °C in air for 4 h with the heating rate of 3 °C/min. For simplicity, a series of as-prepared C–O/CN with different ratios of GLU to DCDA are denoted as C–O/CN-*x* (*x* = 0, 0.05, 0.1, 0.2 and 0.3). For comparison, C, O doped porous g-C₃N₄ nanosheets (C–O/Porous-CN) were prepared as follows: G-D-0.1 solution was centrifuged and dried at 60 °C for 12 h in a vacuum oven. The resulting residue (denoted as G-D-0.1/VD) was collected and transferred into a crucible and pyrolyzed at 520 °C in air for 4 h with the heating rate of 3 °C/min. As reference, bulk-CN was prepared by directly heating DCDA at 520 °C in air for 4 h with the heating rate of 3 °C/min.

2.2. Characterization

The morphology of the samples was examined by scanning electron microscopy (SEM) (JEOL JSM-6701F), transmission electron microscopy (TEM) (Hitachi H-7700) and atomic force microscopy (AFM) (Inspire with PeakForce IR, Bruker Nano Surfaces). An energy-dispersive spectroscopy (EDS) measurement was performed with an X-ray energy dispersive spectrometer installed on a JEOL JSM-6701F microscope. The Brunauer–Emmett–Teller (BET) specific surface area and the Barrett–Joyner–Halenda (BJH) pore-size distribution were taken using a Quantachrome Quadrasorb SI instrument. The crystalline structure of samples was characterized by powder X-ray diffraction (XRD) using Cu K α radiation ($\lambda = 0.15406$ nm) on a Rigaku D/max-2500 VB2+/PC. Electron spin resonance (ESR) spectrum was acquired using a JEOL JES-FA200 X-band spectrometer. ¹³C cross-polarisation magic angle spinning nuclear magnetic resonance spectrum (¹³C NMR) was recorded on a Bruker Avance 300 spectrometer at room temperature. Fourier transform infrared (FT-IR) spectrum was measured on a Bruker Vertex 70 v spectrometer. X-ray photoelectron spectroscopy (XPS) analysis was recorded on a Thermo ESCALAB250 X-ray photoelectron spectrometer using Al K α as an X-ray source. The optical absorption property of samples was determined by using the absorption spectrum performed on a UV–vis spectrophotometer (Perkin Elmer Lambda 950 UV–vis). Photoluminescence (PL) emission and time-resolved spectra were obtained on a Spectrofluorometer FS5 (EDINBURGH INSTRUMENTS) with an excitation wavelength of 340 nm at room temperature.

2.3. Photocatalytic activity measurement

The photocatalytic H₂ production was carried out in a top-irradiation vessel containing 100 mL 10 vol% of triethanolamine (TEOA) aqueous solution. Photocatalyst power (5 mg) with 3 wt% Pt (in situ photo-deposited on the surface as a co-catalyst) was used in the reaction. The reactor was sealed and degassed with N₂ for several times to remove air before irradiated under a 300 W Xe lamp equipped with 420 nm or 470 nm cutoff filter. The amount of evolved H₂ was analyzed by gas chromatography (Agilent 7890B) with high-purity nitrogen carrier gas.

The AQE was measured at 420 nm and 600 nm monochromatic lights which were obtained by using band-pass filters for 1 h. The AQE experiments were carried out using a top-irradiation vessel containing 100 mL 10 vol% of TEOA aqueous solution. Photocatalyst power with 3 wt% Pt (in situ photo-deposited on the surface as a co-catalyst) was used in the reaction. For the AQE at 420 nm, the average intensity of irradiation was determined to be 80 mW/cm² and the irradiation area was 7.5 cm² (exposing a window with a length of 3 cm and width of 2.5 cm). For the AQE at 600 nm, the average intensity of irradiation was measured to be 80 mW/cm² and the irradiation area was also 7.5 cm². The AQE was then calculated by the following Eq. (1):

$$\text{AQE} = \frac{2 \times \text{amount of H}_2 \text{ molecules evolved}}{\text{number of incident photons}} \times 100 \quad (1)$$

2.4. Photoelectrochemical measurements

The photoelectrodes were prepared according to the literature reported previously [31]. The indium doped tin oxide (ITO) substrates were cleaned by ultrasonication in deionized water and absolute ethanol for 15 min, and then dried in an oven. 5 mg of photocatalyst and 10 μ L of Nafion solution (5 wt%) were dispersed in 400 μ L water/isopropanol mixed solvent (3:1 v/v) by 60 min sonication to prepare a homogeneous colloid. Then, all of the catalyst colloid was deposited on the ITO conductive glass with area of 1 cm² and then dried in air to form the working electrode.

The photoelectrochemical properties were investigated in a three-electrode quartz cell with a 0.5 M Na₂SO₄ electrolyte solution; a

platinum wire was used as the counter electrode, a saturated calomel electrode (SCE) was used as the reference electrode, and the as-prepared photocatalyst film was used as the working electrode, respectively. A 300 W Xe lamp equipped with a 420 nm cutoff filter was adopted as a light source. Mott–Schottky plots were obtained under direct current potential polarization at different frequencies (1000, 1200, and 1500 Hz). Electrochemical impedance spectroscopy (EIS) was recorded at an applied potential of 0.01 V versus SCE over the frequency range of 1 MHz to 0.1 Hz.

2.5. Theoretical calculation

The periodic density functional theory (DFT) calculations were employed with the Plane Wave Self-Consistent Field (PWSCF) plane wave code in the Quantum ESPRESSO (QE) package [32]. Generalized gradient approximation (GGA) within the Perdew–Burke–Ernzerhof (PBE) [33] exchange-correction functional and ultrasoft pseudo potentials were used. Monkhorst-pack $3 \times 3 \times 1$ k-point grid was employed.

3. Results and discussion

3.1. Morphology and porous structure

C–O/CN was synthesized by a template-free self-assembly method as schematically illustrated in Fig. 1. Specifically, DCDA (g-C₃N₄ precursor) and GLU (C and O source) were firstly dissolved and then hydrothermally treated in deionized water to obtain a G-D solution. The resultant solution stored in the freezing refrigerator gradually forms ice crystals. Ice crystals then swept along with the solidification front to form parallel ice column and simultaneously left inter column space for the formation of G-D nanobelts [34]. Accompanied with the sublimation of ice via freeze-drying, G-D nanobelts were finally obtained. SEM and TEM images of G-D-0 and G-D-0.1 show obvious belt structure (Fig. S1a & S1c and Fig. S2a & S2c). Further magnified SEM and TEM images show that the nanobelts are composed of sheet-like oligomers (Fig. S1b & S1d and Fig. S2b & S2d). FT-IR spectra of G-D-0 and G-D-0.1 show several strong bands between 1350 and 1700 cm^{−1} and a strong band around 800 cm^{−1} (Fig. S3), corresponding to the characteristic CN heterocycles and the triazine units, and this also means the formation of oligomers [35]. To further investigate the formation of hierarchical nanobelt structure, G-D-0.1/VD was prepared via identical synthetic method with G-D-0.1 except using vacuum drying instead of freeze drying. The SEM images (Fig. S4) reveal that G-D-0.1/VD exhibits common agglomerative sheet-like oligomer structure instead of hierarchical nanobelt structure. Apparently, the generation of hierarchical nanobelt structure of G-D-0.1 originates from oriented growth of ice

crystals in the precursor suspension solution during freezing process. Similar hierarchical architecture has also been observed in the silver nanowire system by ice-mediated freezing process [34].

The hierarchical porous C–O/CN nanobelts were finally obtained by direct calcination of the as-prepared G-D nanobelts in air, accompanied with releasable gas generating and weak bonds breaking during the thermal polycondensation. In SEM images (Fig. 2), it is clear that both C–O/CN-0 and C–O/CN-0.1 are assembled from porous nanosheets interconnecting together as well-defined belts of several of microns in width and tens of microns in length. The local structure of hierarchical porous network is imaged by TEM (Fig. 3 and Fig. S5), where obvious layered porous nanosheets stratified around the surface constituting of integrated belt structure. AFM images further confirm the porous structure of C–O/CN-0.1 nanobelts with an average thickness of ~6 nm (Fig. S6). Particularly, both the SEM and TEM images show that the size of pores for C–O/CN-0.1 are larger than C–O/CN-0, which are ascribed to the introduction of C, O-rich GLU generating more gas during the calcination process.

The specific surface area of bulk-CN and C–O/CN was accessed from the N₂-absorption isotherm (Fig. S7a). The Brunauer–Emmett–Teller specific surface area (S_{BET}) determined for C–O/CN-0 and C–O/CN-0.1 is 107 m² g^{−1} and 120 m² g^{−1}, respectively, which are over 10-times higher than that of bulk-CN (9.6 m² g^{−1}) (Inset in Fig. S7b). The pore size distribution curves (Fig. S7b) indicate that both C–O/CN-0 and C–O/CN-0.1 are rich in pores of diameter between 1 and 50 nm comparing with bulk-CN. Besides, the S_{BET} and pores size of C–O/CN-0.1 are slightly larger than those of C–O/CN-0, which is consistent with the SEM and TEM observations. Such a 10-fold increase in specific surface area of C–O/CN-0 and C–O/CN-0.1 comparing with bulk-CN should be beneficial for its application as photocatalyst because of more exposed interfacial contact sites to the reactants [30,35].

3.2. Chemical states and crystal structure

The XPS analysis was performed to obtain information about the surface compositions and chemical bonding states of bulk-CN, C–O/CN-0 and C–O/CN-0.1. The survey spectra (Fig. S8a) of all samples contain three sharp peaks at around 288 eV, 398 eV and 532 eV, which are assigned to C 1s, N 1s and O 1s, respectively [36]. These indicate that C–O/CN-0 and C–O/CN-0.1 have the chemical composition analogous to bulk-CN. Note that no signal of S 2p is detected in the high-resolution S 2p spectrum of C–O/CN-0.1 (Fig. S8b) because the –SH in GLU is a fast leaving group and S escapes as H₂S during the thermal treatment [37].

The high-resolution C 1s spectra (Fig. 4a) of bulk-CN, C–O/CN-0 and C–O/CN-0.1 can be fitted into four peaks at 288.4 eV, 285 eV,

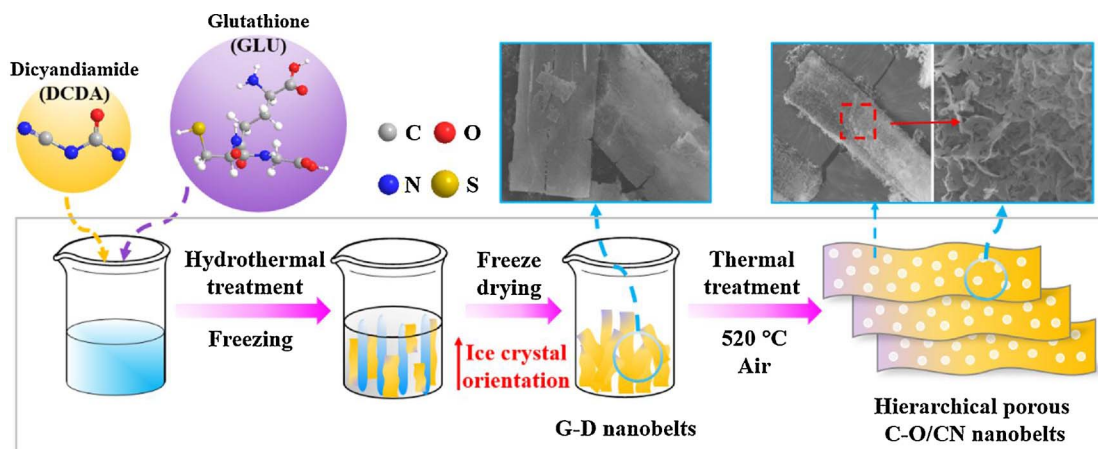


Fig. 1. Schematic illustration for the formation of hierarchical porous C–O/CN nanobelts.

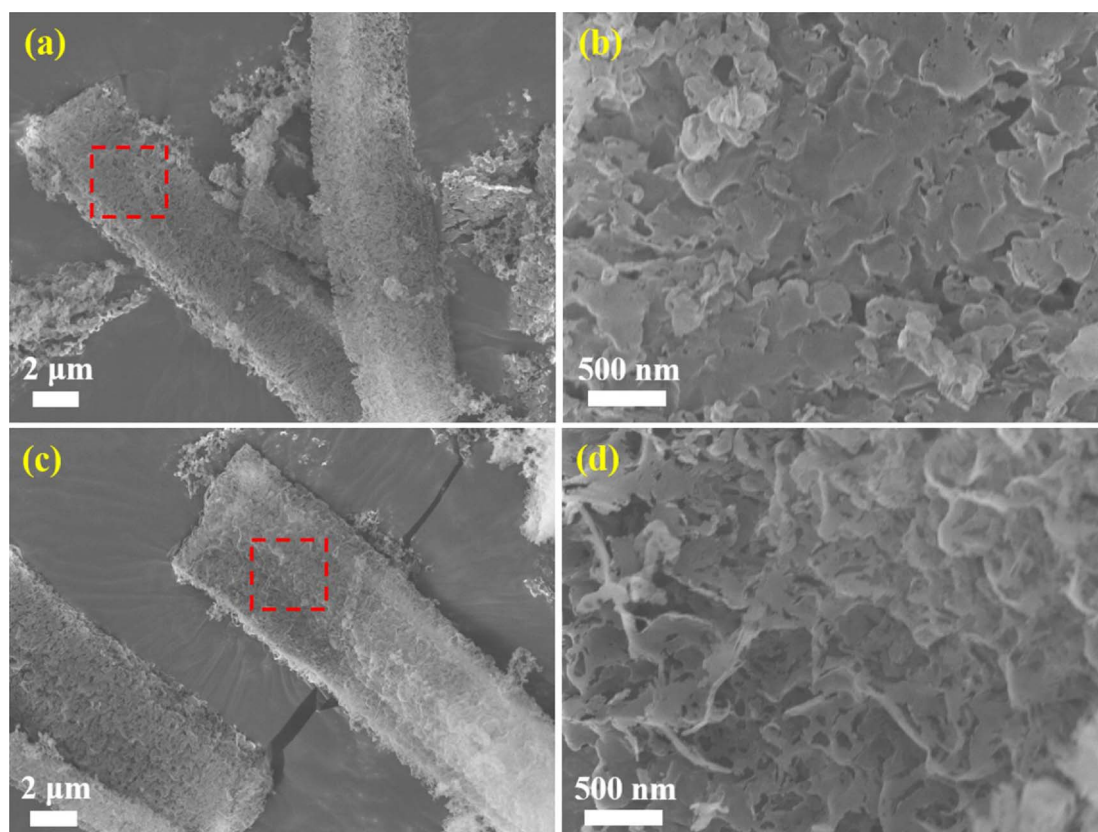


Fig. 2. (a) SEM image of C-O/CN-0, (b) SEM image obtained from the rectangle area of (a); (c) SEM image of C-O/CN-0.1, (d) SEM image obtained from the rectangle area of (c).

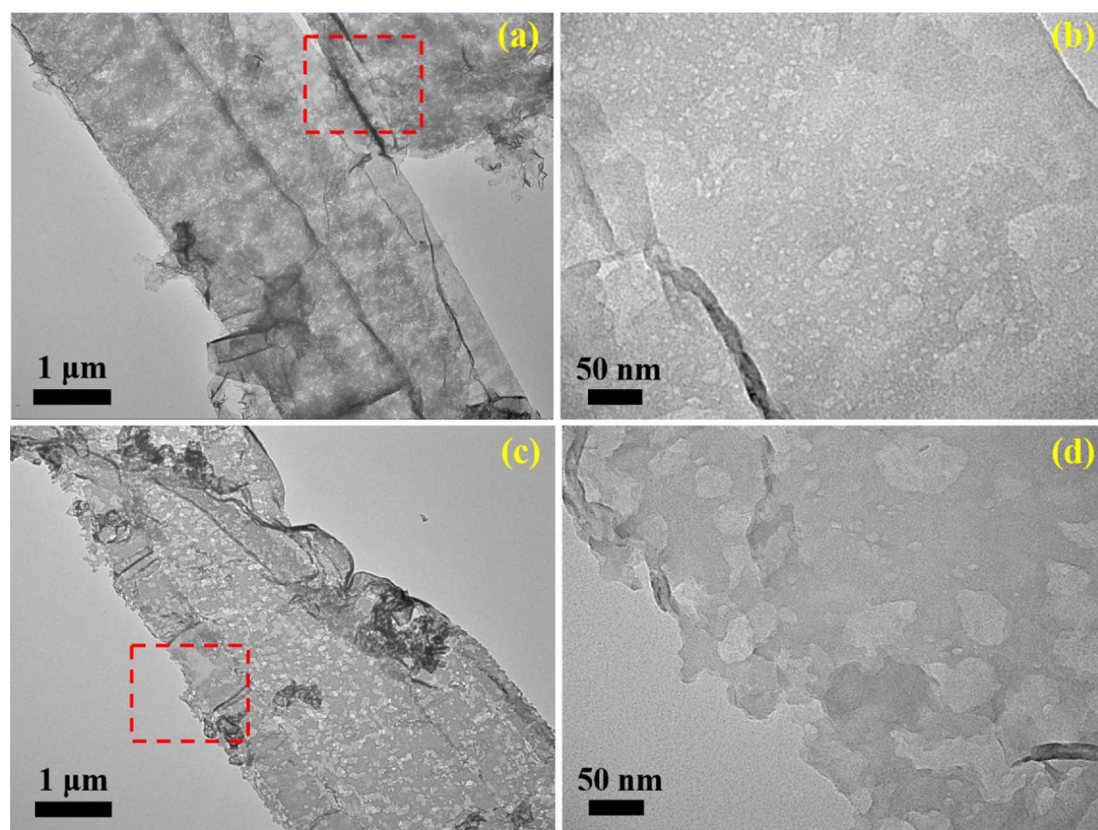


Fig. 3. (a) TEM image of C-O/CN-0, (b) TEM image obtained from the rectangle area of (a); (c) TEM image of C-O/CN-0.1, (d) TEM image obtained from the rectangle area of (c).

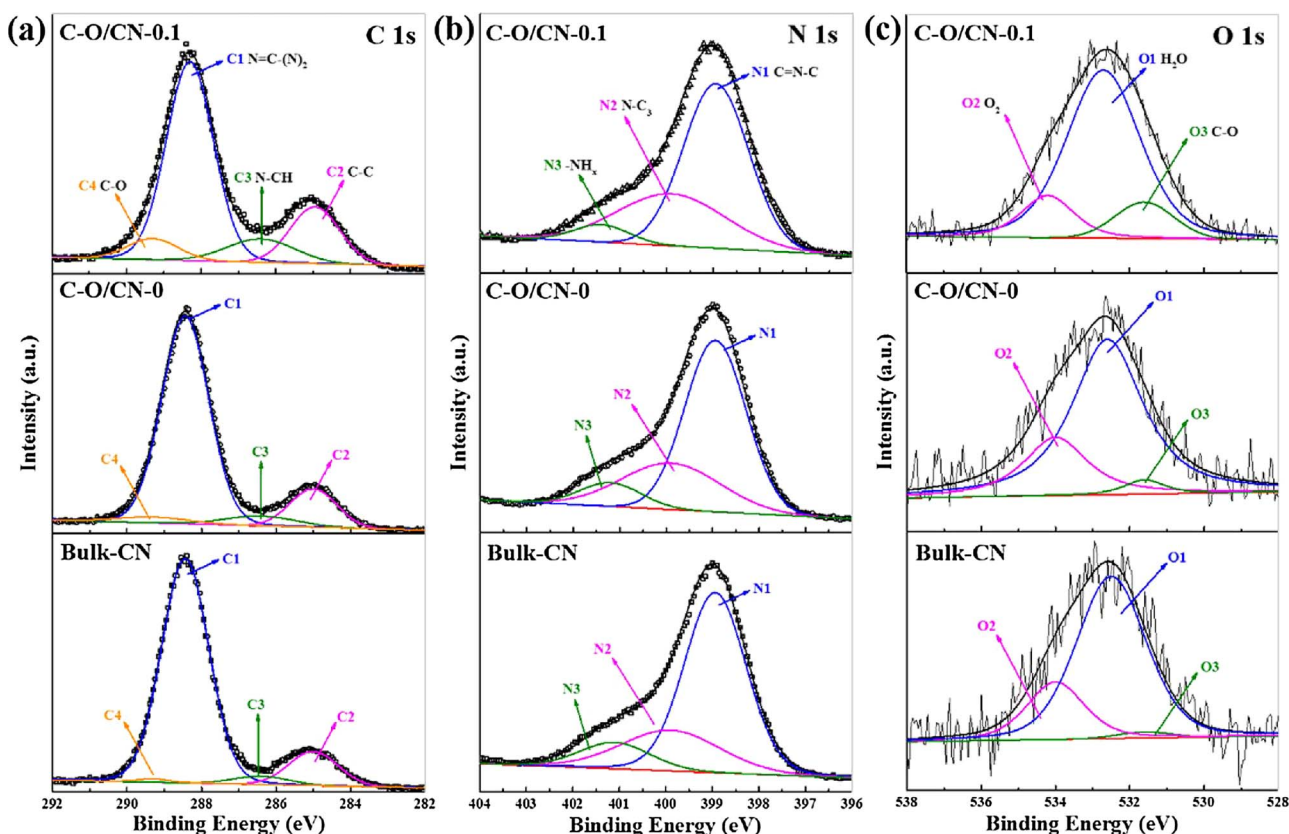


Fig. 4. High-resolution (a) C 1s, (b) N 1s and (c) O 1s XPS spectra of bulk-CN, C-O/CN-0 and C-O/CN-0.1.

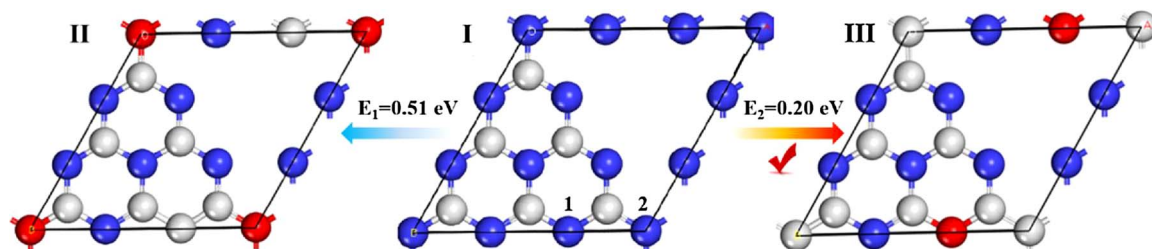


Fig. 5. Calculated formation energy (E) of C, O binary-doped $g\text{-C}_3\text{N}_4$ by substituting N (site 1 and 2) atoms using O and C atom. Top view of the optimized pure $g\text{-C}_3\text{N}_4$ (I); C, O binary-doped $g\text{-C}_3\text{N}_4$ (II, III). Note: C, N and O atom are indicated by gray, blue and red spheres, respectively. (For interpretation of the references to colour in this figure legend, the reader is referred to the web version of this article.)

286.4 eV and 289.3 eV, corresponding to $\text{N}=\text{C}(\text{N}_2)$ coordination in the framework of $g\text{-C}_3\text{N}_4$ (C1), C-C in graphitic carbon species (C2), C-NH on the edges of heptazine unit and adventitious hydrocarbons (C3) and C-O species (C4), respectively [22,38]. It is clearly observed that C/N atomic ratio (Table S1) for C-O/CN-0.1 is 1.05, higher than that for C-O/CN-0 (0.90) and bulk-CN (0.82), which well matches with the EDS results in Fig. S9. Meanwhile, the C1: C2 value for C-O/CN-0.1 is 3.45, lower than that for C-O/CN-0 and bulk-CN (5.66 and 6.57, respectively) (Table S2). The increase of C and N atomic ratio and the decrease of C1: C2 value are believed to be due to substitution of trace amount of N atoms by C atoms in C-O/CN-0.1 [17]. The peak of C3 for C-O/CN-0.1 is found to be higher than that for bulk-CN and C-O/CN-0 (Fig. 4a and Table S2), attributing to surface and edge enhancement [30]. Besides, there is an obviously increased intensity of C4 for C-O/CN-0.1 (Fig. 4a and Table S2), suggesting the increase of C-O groups [22].

The O 1s high-resolution spectra of three samples are shown in Fig. 4c. There are three peaks at 532.6 eV, 534 eV and 531.6 eV, belonging to absorbed H_2O (O1), O_2 (O2) and C-O species (O3), respectively [22]. Besides, we further confirm that there are more C-O

species existent in C-O/CN-0.1 by virtue of the remarkably strong O3 intensity and the greatly enhanced O concentration in C-O/CN-0.1 (Fig. 4c, Table S1 and Table S3).

Apart from the C 1s and O 1s spectra, the N 1s spectra of samples were also investigated for the location of C, O atoms in C-O/CN matrix. As shown in Fig. 4b, the N 1s high-resolution spectra of three samples reveal the existence of the sp^2 -hybridized nitrogen in C-containing triazine rings ($\text{C}=\text{N}-\text{C}$) (N1) at 398.9 eV, the inner N atoms bonded with three sp^2 carbon atoms $\text{N}-\text{C}_3$ (N2) at 399.9 eV and $-\text{NH}_x$ groups (N3) at 401.2 eV [29,38]. The decreased area ratio of N1 from bulk-CN to C-O/CN-0.1 (Table S4) confirms the replacement of trace amount sp^2 -hybridized N in C-containing triazine rings with C or O because of C and O doping [11,13,17,20]. Furthermore, the discernible decrease in intensity and the slight increase in binding energy of N3 for C-O/CN-0.1 occur (Fig. 4b and Table S4) suggest that C or O atoms probably replaces trace amount of N atoms in $-\text{NH}_x$ groups (N3) to form C-C or C-O bonds [18,22,39,40] (Fig. 5).

DFT calculations further confirmed the specific doping locations of C and O. Two possible substitution sites of N atoms are numbered as 1 and 2. The formation energy (E) of substitutional C atom in site 1 and O

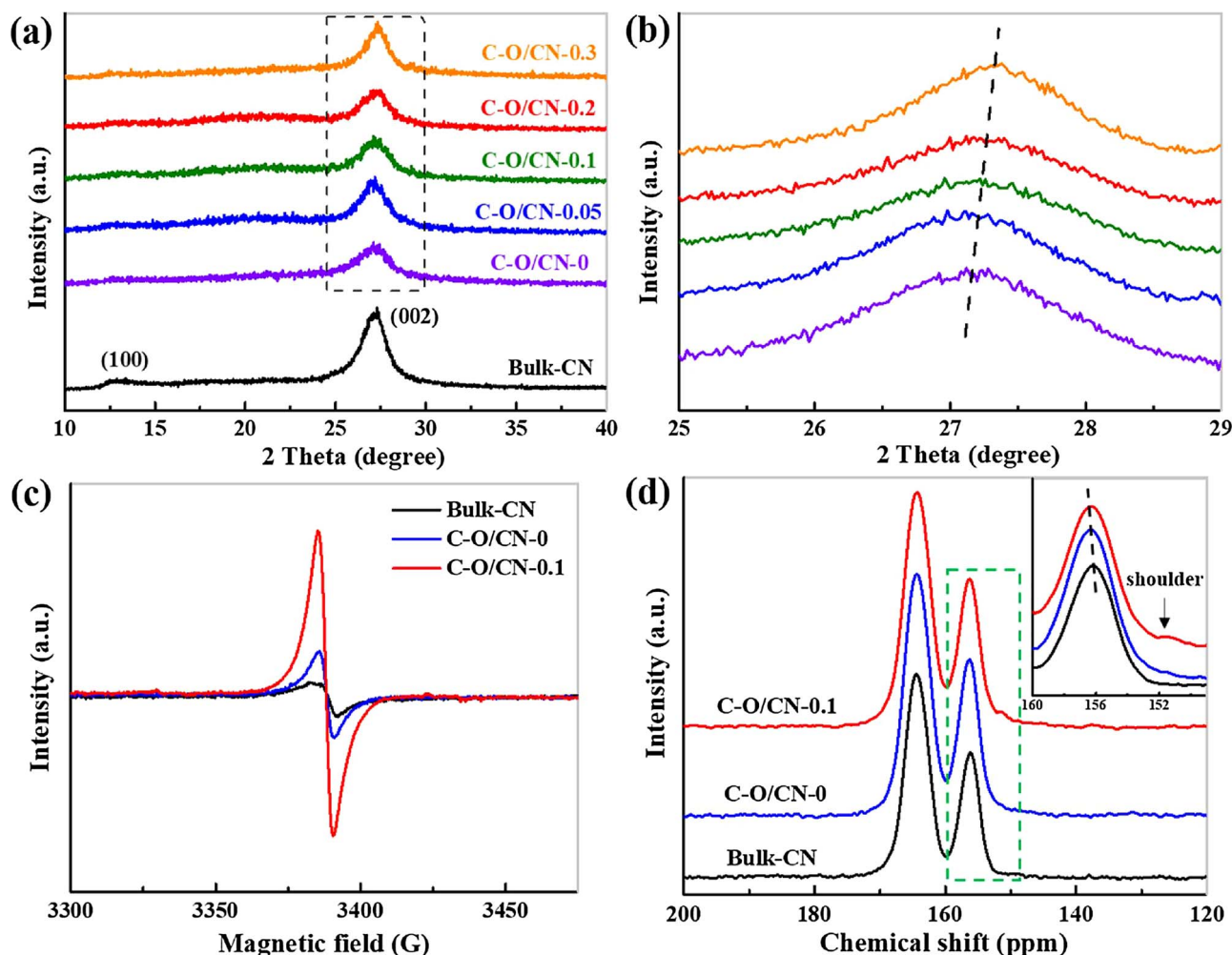


Fig. 6. XRD patterns of (a) bulk-CN and C-O/CN-x ($x=0, 0.05, 0.1, 0.2$ and 0.3) and (b) magnified peaks at (002) of C-O/CN-x. (c) ESR spectra of bulk-CN, C-O/CN-0 and C-O/CN-0.1. (d) ^{13}C NMR spectra of bulk-CN, C-O/CN-0 and C-O/CN-0.1. Inset: the magnified region of the rectangle area.

atom in site 2 is 0.51 eV whereas substitutional C atom in site 2 and O atom in site 1 is 0.20 eV. Thus, the substitution of N atom in site 1 with O atom and site 2 with C atom is more favorable based on lower formation energy [13,41].

The crystal structure of bulk-CN and a series of C-O/CN-x ($x=0, 0.05, 0.1, 0.2$ and 0.3) porous nanobelts was characterized by XRD. The XRD pattern of bulk-CN features two characteristic peaks (Fig. 6a) at 12.7° (100) and 27.2° (002) relating to the in-plane tri-s-triazine motif and the interlayer stacking reflection of conjugated aromatic segments, respectively [42,43]. The C-O/CN-x show similar XRD patterns with bulk-CN, suggesting that C-O/CN-x share identical crystal structure with bulk-CN. Remarkably, the peak of (100) is weaker for C-O/CN-x, suggesting less ordered stacking of tri-s-triazine motifs. This is understandable because of the substitution of N atoms by C or O atoms and the formation of hierarchical porous architecture affecting the arrangement of in-plane structure [19,35]. Additionally, with increasing GLU usage, the peak of (002) shows regularly shift toward higher angles in the magnified view of (002) diffraction peak (from 27.12° for C-O/CN-0 to 27.35° for C-O/CN-0.3) (Fig. 6b, Table S5). According to Bragg's law [44], the increase in 2θ values indicates a slightly narrowed interlayer distance i.e. from 3.285 for C-O/CN-0 to 3.259 for C-O/CN-0.3 (Table S5), which can be interpreted as the consequential disturbance of graphitic structure after the partial replacement of N atoms by C atoms [17,22]. Comparing with N atom, C atom owns one less valence electron and O atom has one more valence electron. As such, the substitution of N atoms by C and O atoms in different sites would

cause the formation of unpaired electrons [22]. The spin state of unpaired electrons can be measured by ESR technique. Fig. 6c shows that bulk-CN, C-O/CN-0 and C-O/CN-0.1 exhibit one single Lorentzian line with a g value of 2.0034 due to long pair electrons in sp^2 -carbon in a typical heptazine graphitic carbon nitride [16]. In comparison with bulk-CN, the ESR intensity of C-O/CN-0 is slightly enhanced, and this may be ascribed to the increase of defect sites of C-O/CN-0 with enhanced surface area [20]. Particularly, C-O/CN-0.1 exhibits the greatly strengthened ESR intensity among three samples, and this implied the formation of increased unpaired spin electrons by the replacement of N atom by C and O atoms in the heptazine unit [16,22]. The ^{13}C NMR was employed to investigate the chemical state of C (Fig. 6d). The NMR spectra of bulk-CN, C-O/CN-0 and C-O/CN-0.1 show two strong peaks at 164.3 and 156.3 ppm corresponding to the chemical shifts of $\text{CN}_2\text{-NH}_x$ and CN_3 in g- C_3N_4 , respectively [45]. The peak at 156.3 ppm of C-O/CN-0.1 shows slightly higher chemical shift and a shoulder at 151.3 ppm, suggesting the appearance of new state C atoms in the g- C_3N_4 matrix.

From FT-IR spectra (Fig. S10a), one can see that C-O/CN exhibits several typical stretching modes of CN heterocycles in $1700\text{--}1200\text{ cm}^{-1}$ and a peak at approximately 810 cm^{-1} originating from the typical out-of-plane bending vibration characteristic of the tri-s-triazine unit, indicating that C-O/CN maintains the core g- C_3N_4 heterocycle structure similar to bulk-CN [19]. Moreover, comparing with bulk-CN, the peaks of C-O/CN in $3700\text{--}2900\text{ cm}^{-1}$ apparently increase and this indicates the more enlarged open-up surfaces in the C-O/CN texture structure

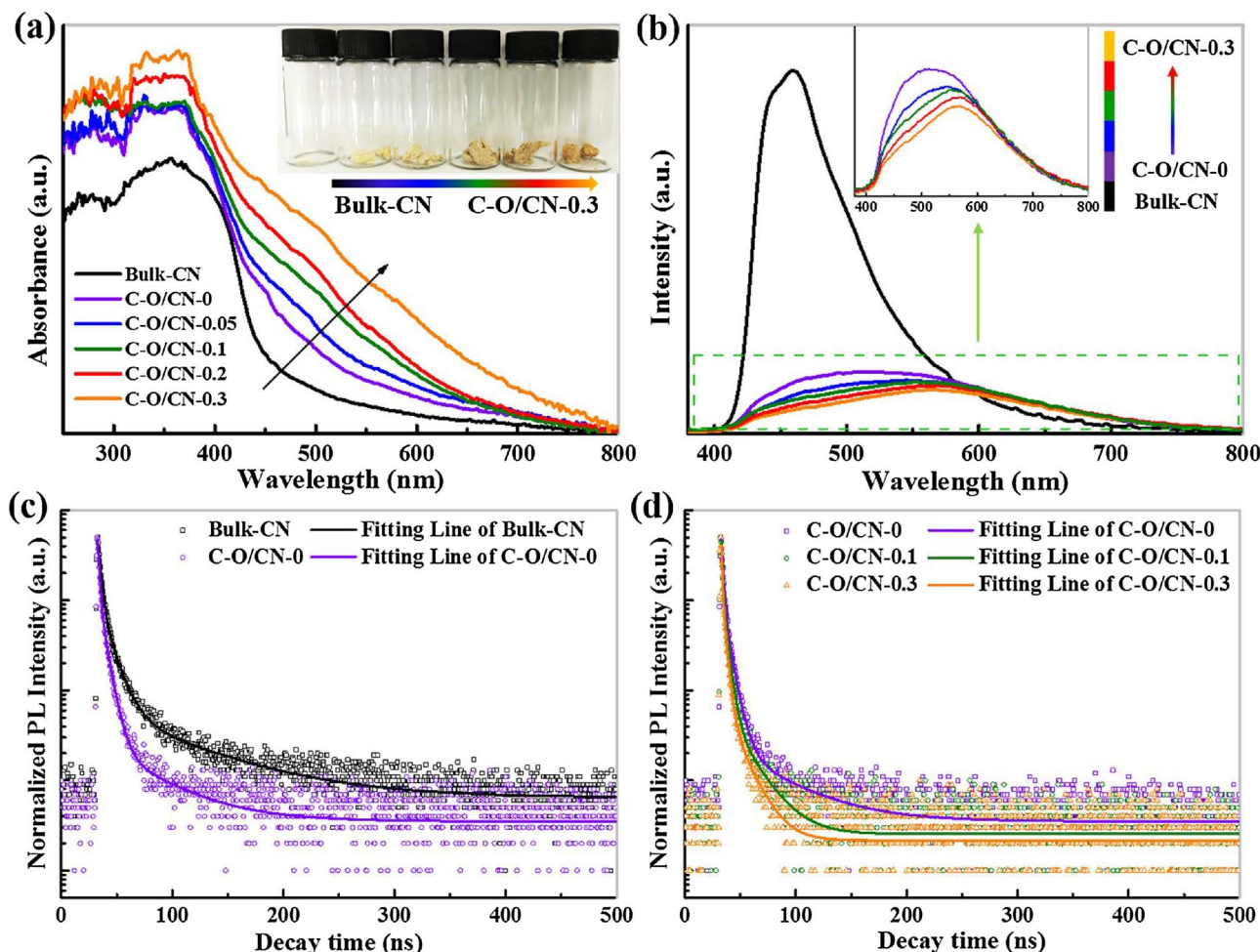


Fig. 7. (a) UV-vis spectra of bulk-CN and C-O/CN-*x* (*x* = 0, 0.05, 0.1, 0.2 and 0.3), (b) PL spectra of bulk-CN and C-O/CN-*x*. Inset: the magnified region of the rectangle area. Time-resolved PL spectra of (c) bulk-CN and C-O/CN-0 and (d) C-O/CN-0, C-O/CN-0.1 and C-O/CN-0.3.

[30,35]. Further, compared with 810 cm^{-1} peak in C-O/CN-0, there is a 3 cm^{-1} shift to high frequencies in C-O/CN-0.1 (Fig. S10b), suggesting that interaction weakened between the “nitrogen pots” in C-O/CN-0.1 due to the substitution of N atoms by C and O atoms [22]. Besides, XPS and EDS results show that comparing with bulk-CN, N concentration of C-O/CN-0.1 decreases. This decrease is most likely to be due to the replacement of N atoms by C and O atoms rather than from N vacancies because no peaks of N vacancies were detected in the FT-IR spectrum of C-O/CN-0.1 (Fig. S10).

3.3. Optical and photoelectric properties and electronic-band structure

The optical and photoelectric properties of bulk-CN and C-O/CN-*x* were characterized by UV-vis spectra, PL emission spectra, time-resolved PL spectra, photocurrent transient responses and EIS. From inset in Fig. 7a, one can see that with increasing GLU usage, the C-O/CN-*x* progressively becomes dark yellow from a yellowish color, and compared with bulk-CN (same mass of 5 mg), the volume of C-O/CN-*x* becomes larger. UV-vis spectra in Fig. 7a show a progressive redshift of the absorption edge as well as broader and stronger absorption tails with increasing GLU usage. Bandgaps of all samples are acquired by the Kubelk-Munk method (Fig. S11) [38]. Clearly, the bandgap energies increase from 2.78 eV (bulk-CN) to 2.80 eV (C-O/CN-0) as hierarchical porous nanobelt structure forms. Such an increase in the bandgap energy could be explained by the quantum confinement effect of C-O/CN-0 [28]. Upon continuously increasing GLU usage, bandgap energies of C-O/CN-*x* narrow from 2.80 eV to 2.45 eV, and this could be

predominantly ascribed to the partial substitution of the N atoms by C and O atoms.

Apart from light absorption, photo-excited electron-hole separation and charge transfer also play a pivotal role in photocatalysis. PL emission spectra technology is a powerful tool to characterize the radiative recombination process of photo-excited charge transfer in the samples [9,20]. As shown in Fig. 7b, in contrast to a strong fluorescence emission peak at 460 nm exhibited by bulk-CN, C-O/CN-0 present much quenched PL signals, indicating more efficient charge separation and transfer within hierarchical porous nanobelt structure. Also, this deduction is corroborated by time-resolved PL decay spectra (Fig. 7c). The PL lifetimes of bulk-CN and C-O/CN-0 are calculated by fitting the time-resolved PL decay curves with the following exponential fitting Eq. (2):

$$Fit = A + B_1 \exp\left\{-\frac{t}{\tau_1}\right\} + B_2 \exp\left\{-\frac{t}{\tau_2}\right\} \quad (2)$$

where A , B_1 , B_2 , are constants and obtained after fitting every decay curve. Simultaneously, a fast (τ_1) and a slow (τ_2) decay component can be obtained from the above equation [9]. Then, on the basis of the fitting data, the average life-time (τ_{avg}) is calculated by following Eq. (3):

$$\tau_{avg} = \frac{B_1 \tau_1^2 + B_2 \tau_2^2}{B_1 \tau_1 + B_2 \tau_2} \quad (3)$$

The fitting PL decay data (B_1 , B_2 , τ_1 , τ_2 and χ^2) and average life-time (τ_{avg}) of bulk-CN and C-O/CN-0 are summarized and listed in

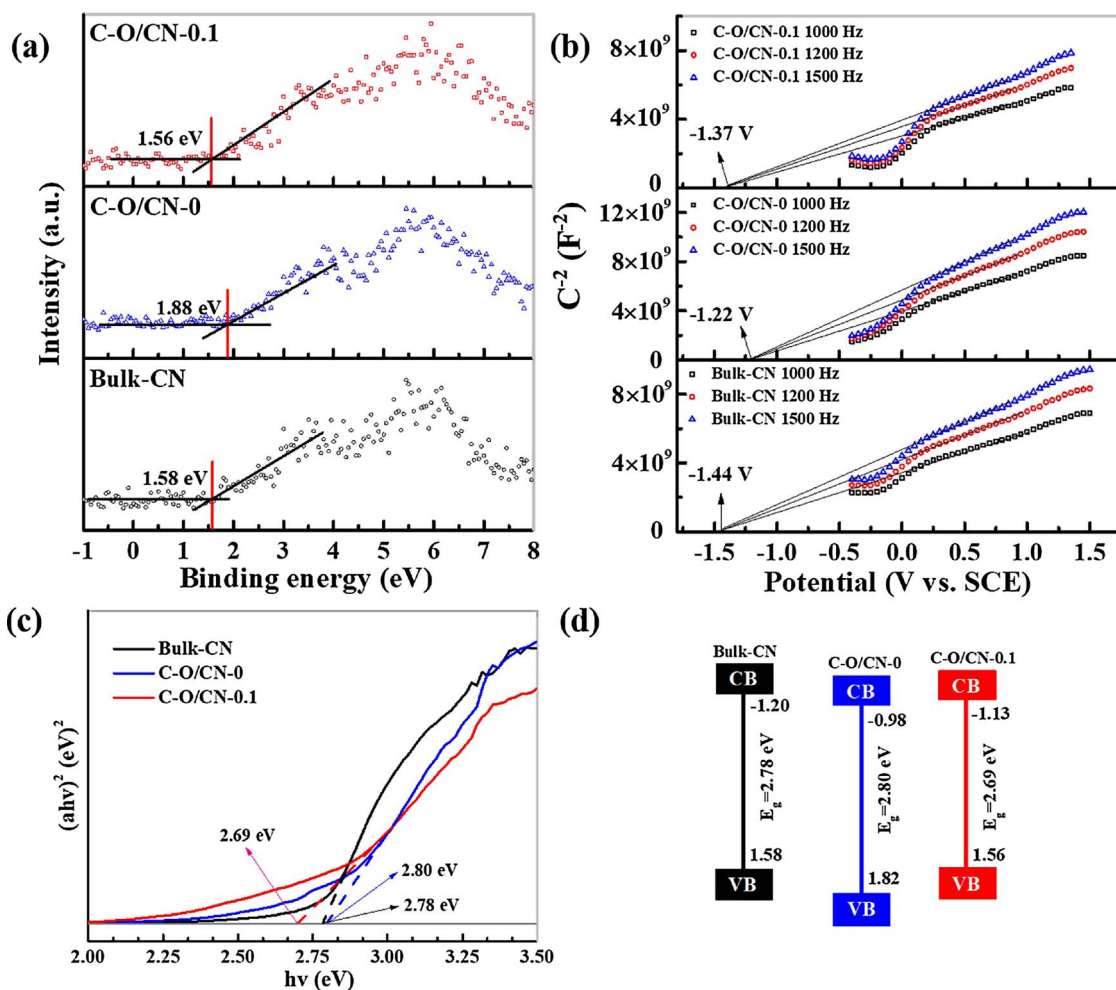


Fig. 8. High resolution valence band XPS spectra (a), Mott-Schottky plots (b), schematic illustration of the bandgap (c) and schematic illustration of the band structure (d) of bulk-CN, C-O/CN-0 and C-O/CN-0.1. Note: the flat-band position of bulk-CN, C-O/CN-0 and C-O/CN-0.1 in (b) are estimated to be at -1.44 V, -1.22 V and -1.37 V vs. saturated calomel electrode (SCE) at pH=7, which correspond to -1.20 V, -0.98 V and -1.13 V vs. standard hydrogen electrode (SHE) at pH=0, respectively.

Table S6. According to the calculated results, the τ_{avg} of charge carries decreases from 6.28 ns of bulk-CN to 3.71 ns of C-O/CN-0. The lower τ_{avg} implies the efficient charge separation and transfer occurring in open-framework porous nanobelt structure of C-O/CN-0 [20].

Moreover, with the increasing GLU usage, PL signal of C-O/CN-x progressively lose intensity and show redshift (Inset in Fig. 7b) and the τ_{avg} of charge transfer decrease from 3.71 ns for C-O/CN-0 to 2.03 ns for C-O/CN-0.3 (Fig. 7d, Fig. S12 and Table S6). The redshift of signals is probably attributed to the narrowing of bandgaps for C-O/CN-x materials [46]. The quenched PL signals and decreased τ_{avg} of charge transfer after C, O doping indicate that the energy-wasteful charge recombination is substantially suppressed and thus improving charge separation and transfer [20,35]. Additionally, the discernibly increased photocurrent under visible-light (Fig. S13) and the decreased Nyquist plots diameter (Fig. S14) also indicate the enhancement in the charge separation and transfer efficiency of C-O/CN-0.1 [38,47].

To reveal whether the hierarchical porous design and C, O doping can promote the photocatalytic H_2 production, it is necessary to calculate their energy band positions [9]. The Mott-Schottky analysis was used to determine the flat-band potential of samples (Fig. 8b). The Mott-Schottky plots of all samples under various frequencies exhibit the positive slope in the linear region, indicating they are n-type semiconductors [48]. More importantly, the flat-band position of bulk-CN, C-O/CN-0 and C-O/CN-0.1 are estimated to be at -1.44 V, -1.22 V and -1.37 V vs. saturated calomel electrode (SCE) at pH = 7, which correspond to -1.20 V, -0.98 V and -1.13 V vs. standard

hydrogen electrode (SHE) at pH = 0, respectively [49], indicating all of the samples thermodynamically enable photocatalytic reduction of water ($2H^+ + 2e^- = H_2$, $E_0 = 0$ V vs. SHE) [9]. The valence band (VB) position of samples was measured by valence band XPS spectra. As show in Fig. 8a, the VB position of bulk-CN, C-O/CN-0 and C-O/CN-0.1 is estimated to be at 1.58 eV, 1.88 eV and 1.56 eV, respectively. Based on the above data and combined with the bandgap energies (Fig. 8c), the band structure of bulk-CN, C-O/CN-0 and C-O/CN-0.1 can be obtained (Fig. 8d). Obviously, with the morphology changing from bulk to hierarchical porous nanobelt, the CB and VB down shift to a more positive position, which is harmful for photocatalytic reaction because of the decreased reduction driving force for H_2 evolution [38]. By contrast, when C, O atoms are introduced to the catalyst, the CB and VB positions of C-O/CN-0.1 give rise to negative shifts and at the same time the bandgap narrowing of C-O/CN-0.1 occurs. The more negative position of CB and narrower bandgap can enhance the reduction capability of electrons and visible-light response, which are beneficial for the facilitating of H_2 evolution [44].

3.4. Photocatalytic performance

To assess the photocatalytic performance of hierarchical porous C, O binary-doped g-C₃N₄ nanobelts, the photocatalytic H_2 evolution was performed under visible-light irradiation, using TEOA as electron donor and 3 wt% Pt as co-catalyst. Fig. 9a shows the comparison of photocatalytic H_2 production performance of bulk-CN, C-O/CN-0 and C-O/CN-0.1.

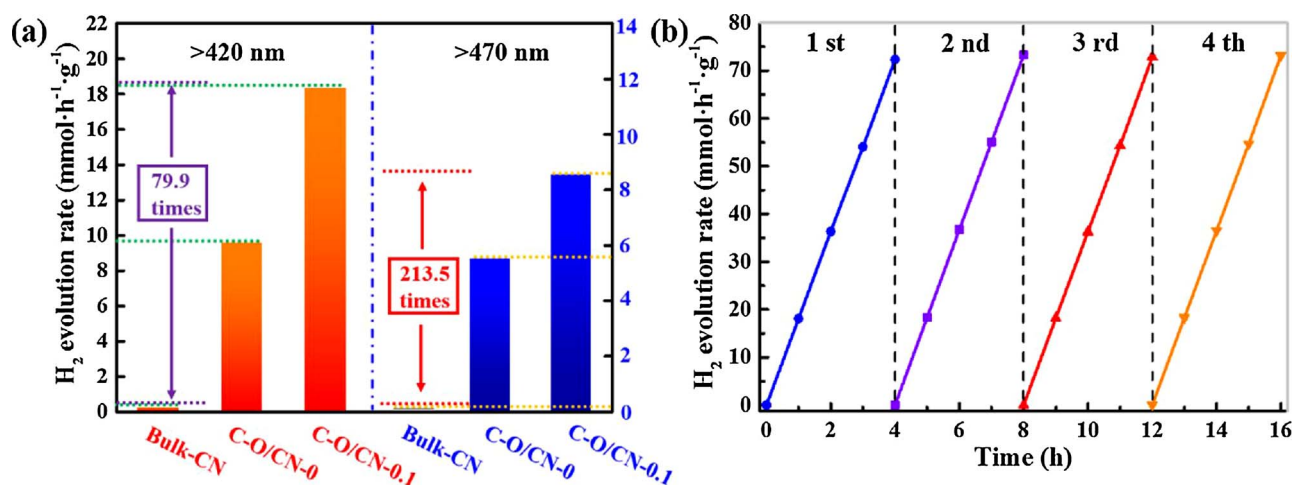


Fig. 9. Photocatalytic H₂ evolution rate of (a) bulk-CN, C-O/CN-0 and C-O/CN-0.1 with 3 wt% Pt under visible-light irradiation ($\lambda > 420$ nm and $\lambda > 470$ nm), and (b) recycle of H₂ evolution of C-O/CN-0.1.

CN-0.1 under visible-light irradiation ($\lambda > 420$ nm and $\lambda > 470$ nm). The H₂ evolution rate of bulk-CN is the lowest of three samples ($0.23 \text{ mmol h}^{-1} \text{ g}^{-1}$ for $\lambda > 420$ nm and $0.04 \text{ mmol h}^{-1} \text{ g}^{-1}$ for $\lambda > 470$ nm), attributing to the intrinsic drawbacks (poor surface area, unsatisfactory visible-light harvesting and rapid recombination of photo-excited charge transfer). After the formation of hierarchical porous nanobelt structure, the H₂ production activity of C-O/CN-0 increases obviously comparing with bulk-CN. The H₂ evolution rate of the C-O/CN-x increases with the mass ratio of GLU to DCDA up to 0.1%. Further increase the mass ratio to 0.3% gives rise to a decrease of H₂ evolution rate because the excess amounts of dopants will distort the conduction path and thus offer more potential recombination sites (Fig. S15) [50,51]. Remarkably, C-O/CN-0.1 shows the highest H₂ evolution of $18.38 \text{ mmol h}^{-1} \text{ g}^{-1}$ under $\lambda > 420$ nm visible-light irradiation, which is about 1.92 times than that of C-O/CN-0 ($9.59 \text{ mmol h}^{-1} \text{ g}^{-1}$) and 79.9-fold than that of bulk-CN ($0.23 \text{ mmol h}^{-1} \text{ g}^{-1}$). Simultaneously, the H₂ evolution rate of C-O/CN-0.1 under $\lambda > 470$ nm visible-light irradiation is also tremendously increased to $8.54 \text{ mmol h}^{-1} \text{ g}^{-1}$, which is about 123.5 times higher than that of bulk-CN ($0.04 \text{ mmol h}^{-1} \text{ g}^{-1}$). To further prove the superiority of this C, O binary-doping hierarchical nanobelt structure for photocatalytic H₂ production, we compared the H₂ evolution rate of C-O/CN-x with other representative photocatalysts (Fig. S16). It is clear that the photocatalytic activity of C-O/CN-0.1 is much higher than that of P25, C-CN and O-CN. Simultaneously, it is worth noting that C-O/CN-0.1 displays a higher H₂ evolution rate than C-O/porous-CN (Fig. S17), demonstrating the advantage of the hierarchical nanobelt structure. Besides, the calculated apparent quantum efficiency (AQE) for C-O/CN-0.1 is 9.83% under irradiation at 420 nm, which is higher than that of C-O/CN-0 (5.82%) and the bulk-CN (0.12%). Surprisingly, C-O/CN-0.1 shows an AQE of 0.95% at 600 nm. In contrast, bulk-CN shows no AQE at the wavelength of 600 nm because of limit light absorption at such a wavelength (Table S7). To the best of our knowledge, the visible-light-driven H₂ evolution rate and AQE of C-O/CN-0.1 are higher than most of previously reported hierarchical structure and non-metal doped g-C₃N₄ photocatalysts and accordingly comparative data and results are summarized and listed in Table S8. The pronounced enhancement of H₂ evolution and AQE can be attributed to the following reasons. Firstly, the larger specific surface area of the hierarchical porous C-O/CN-0.1 nanobelt leads to expose more interfacial as active reduction sites for H₂ evolution compared to bulk-CN (see results and discussion of SEM, TEM and BET). Secondly, C-O/CN-0.1 with partial substitution of N atoms by C and O atoms exhibits a more negative CB position and narrower bandgap than bulk-CN, resulting in stronger reduction capability of electrons and more effective visible-light harvesting for H₂ production.

Additionally, compared with bulk-CN, C-O/CN-0.1 nanobelt with abundant interconnected pore network and optimized electronic-band structure, can geometrically shorten the diffusion distance of the photo-excited charge from the interior to the edges of layer, which favours photocatalytic H₂ production by decreasing the recombination probability of photo-excited electron-hole and promoting charge transfer (see results and discussion of photoelectric properties).

Additionally, the stability of C-O/CN was also investigated in order to demonstrate its practical applicability in photocatalysis [52]. As shown in Fig. 9b, the amount of H₂ yield over C-O/CN-0.1 is almost in proportion to the reaction time within 16 h under visible-light irradiation ($\lambda > 420$ nm). Moreover, the TEM, SEM, XRD and XPS data after the stability test (Fig. S18) show no obvious change, indicating the robustness of C-O/CN-0.1.

4. Conclusions

In conclusion, C-O/CN with hierarchical porous nanobelt architecture was successfully synthesized by a straightforward and eco-friendly template-free self-assembly method, using GLU as C and O source. The resultant C-O/CN exhibits unusual hierarchical nanobelt architecture composed of porous nanosheets, resulting in obvious enhanced specific surface area ($120 \text{ m}^2 \text{ g}^{-1}$) compared with bulk-CN ($9.6 \text{ m}^2 \text{ g}^{-1}$). Additionally, C, O heteroatoms doping, introduced into the structure of g-C₃N₄ by substituting N atoms in $-\text{NH}_x$ groups and triazine rings respectively, cause narrowed bandgap for more effective visible-light harvesting and negatively shifted conduction band position for stronger reducibility of electrons for H₂ production. Simultaneously, the efficiency of charge separation and transfer for hierarchical porous C-O/CN nanobelts are demonstrated to be highly enhanced. As a consequence, the C-O/CN exhibits remarkably enhanced visible-light (> 420 nm) photocatalytic H₂ production rate of $18.38 \text{ mmol h}^{-1} \text{ g}^{-1}$ and AQE of 9.83% at 420 nm and 0.95% at 600 nm. This work provides an easy and green route to prepare a high-efficiency heteroatoms binary-doped hierarchical porous g-C₃N₄ photocatalyst.

Acknowledgements

The work was supported by the National Natural Science Foundation of China (Nos. 21377011, 21476019, 21676017). The authors also thanked Dapeng Cao and Lin Zhu for helping in theoretical calculation.

Appendix A. Supplementary data

Supplementary data associated with this article can be found, in the online version, at <https://doi.org/10.1016/j.apcatb.2017.12.045>.

References

- [1] W.J. Ong, L.L. Tan, Y.H. Ng, S.T. Yong, S.P. Chai, *Chem. Rev.* 116 (2016) 7159–7329.
- [2] X. Wang, K. Maeda, A. Thomas, K. Takanabe, G. Xin, J.M. Carlsson, K. Domen, M. Antonietti, *Nat. Mater.* 8 (2009) 76–80.
- [3] X. Wang, G. Sun, N. Li, P. Chen, *Chem. Soc. Rev.* 45 (2016) 2239–2262.
- [4] L. Jiang, X. Yuan, Y. Pan, J. Liang, G. Zeng, Z. Wu, H. Wang, *Appl. Catal. B: Environ.* 217 (2017) 388–406.
- [5] G. Dong, L. Yang, F. Wang, L. Zang, C. Wang, *ACS Catal.* 6 (2016) 6511–6519.
- [6] R. Ye, H. Fang, Y.Z. Zheng, N. Li, Y. Wang, X. Tao, *ACS Appl. Mater. Interfaces* 8 (2016) 13879–13889.
- [7] K. Chen, Z. Chai, C. Li, L. Shi, M. Liu, Q. Xie, Y. Zhang, D. Xu, A. Manivannan, Z. Liu, *ACS Nano* 10 (2016) 3665–3673.
- [8] Y. Wang, H. Wang, F. Chen, F. Cao, X. Zhao, S. Meng, Y. Cui, *Appl. Catal. B: Environ.* 206 (2017) 417–425.
- [9] J. Ran, T.Y. Ma, G. Gao, X.-W. Du, S.Z. Qiao, *Energy Environ. Sci.* 8 (2015) 3708–3717.
- [10] Z. Lin, X. Wang, *Angew. Chem. Int. Ed.* 52 (2013) 1735–1738.
- [11] G. Dong, K. Zhao, L. Zhang, *Chem. Commun.* 48 (2012) 6178–6180.
- [12] J. Fang, H. Fan, M. Li, C. Long, *J. Mater. Chem. A* 3 (2015) 13819–13826.
- [13] Z.-F. Huang, J. Song, L. Pan, Z. Wang, X. Zhang, J.-J. Zou, W. Mi, X. Zhang, L. Wang, *Nano Energy* 12 (2015) 646–656.
- [14] K. Wang, Q. Li, B. Liu, B. Cheng, W. Ho, J. Yu, *Appl. Catal. B: Environ.* 176–177 (2015) 44–52.
- [15] Y.-P. Zhu, T.-Z. Ren, Z.-Y. Yuan, *ACS Appl. Mater. Interfaces* 7 (2015) 16850–16856.
- [16] G. Zhang, M. Zhang, X. Ye, X. Qiu, S. Lin, X. Wang, *Adv. Mater.* 26 (2014) 805–809.
- [17] Y. Ding, Y. Tang, L. Yang, Y. Zeng, J. Yuan, T. Liu, S. Zhang, C. Liu, S. Luo, *J. Mater. Chem. A* 4 (2016) 14307–14315.
- [18] Z. Zhao, Y. Sun, F. Dong, Y. Zhang, H. Zhao, *RSC Adv.* 5 (2015) 39549–39556.
- [19] J. Fu, B. Zhu, C. Jiang, B. Cheng, W. You, J. Yu, *Small* 13 (2017).
- [20] P. Qiu, C. Xu, H. Chen, F. Jiang, X. Wang, R. Lu, X. Zhang, *Appl. Catal. B: Environ.* 206 (2017) 319–327.
- [21] X. She, L. Liu, H. Ji, Z. Mo, Y. Li, L. Huang, D. Du, H. Xu, H. Li, *Appl. Catal. B: Environ.* 187 (2016) 144–153.
- [22] L. Yang, J. Huang, L. Shi, L. Cao, Q. Yu, Y. Jie, J. Fei, H. Ouyang, J. Ye, *Appl. Catal. B: Environ.* 204 (2017) 335–345.
- [23] L. Jiang, X. Yuan, G. Zeng, X. Chen, Z. Wu, J. Liang, J. Zhang, H. Wang, H. Wang, *ACS Sustain. Chem. Eng.* 5 (2017) 5831–5841.
- [24] H. Wang, B. Wang, Y. Bian, L. Dai, *ACS Appl. Mater. Interfaces* 9 (2017) 21730–21737.
- [25] H. Ma, Y. Li, S. Li, N. Liu, *Appl. Surf. Sci.* 357 (2015) 131–138.
- [26] S. Guo, Y. Zhu, Y. Yan, Y. Min, J. Fan, Q. Xu, *Appl. Catal. B: Environ.* 185 (2016) 315–321.
- [27] Q. Liang, Z. Li, X. Yu, Z.H. Huang, F. Kang, Q.H. Yang, *Adv. Mater.* 27 (2015) 4634–4639.
- [28] Q. Han, B. Wang, J. Gao, Z. Cheng, Y. Zhao, Z. Zhang, L. Qu, *ACS Nano* 10 (2016) 2745–2751.
- [29] Q. Han, B. Wang, J. Gao, L. Qu, *Angew. Chem. Int. Ed.* 55 (2016) 10849–10853.
- [30] J. Zhang, M. Zhang, C. Yang, X. Wang, *Adv. Mater.* 26 (2014) 4121–4126.
- [31] G. Liu, G. Zhao, W. Zhou, Y. Liu, H. Pang, H. Zhang, D. Hao, X. Meng, P. Li, T. Kako, J. Ye, *Adv. Funct. Mater.* 26 (2016) 6822–6829.
- [32] P. Giannozzi, S. Baroni, N. Bonini, M. Calandra, R. Car, C. Cavazzoni, D. Ceresoli, G.L. Chiarotti, M. Cococcioni, I. Dabo, *J. Phys.: Condens. Matter* 21 (2009) 395502.
- [33] J.P. Perdew, K. Burke, M. Ernzerhof, *Phys. Rev. Lett.* 77 (1996) 3865.
- [34] H.L. Gao, L. Xu, F. Long, Z. Pan, Y.X. Du, Y. Lu, J. Ge, S.H. Yu, *Angew. Chem. Int. Ed.* 53 (2014) 4561–4566.
- [35] Q. Han, B. Wang, Y. Zhao, C. Hu, L. Qu, *Angew. Chem. Int. Ed.* 54 (2015) 11433–11437.
- [36] J. Liu, Y. Liu, N. Liu, Y. Han, X. Zhang, H. Huang, Y. Lifshitz, S.-T. Lee, J. Zhong, Z. Kang, *Science* 347 (2015) 970–974.
- [37] Y. Cui, J. Zhang, G. Zhang, J. Huang, P. Liu, M. Antonietti, X. Wang, *J. Mater. Chem.* 21 (2011) 13032.
- [38] H. Yu, R. Shi, Y. Zhao, T. Bian, Y. Zhao, C. Zhou, G.I.N. Waterhouse, L.Z. Wu, C.H. Tung, T. Zhang, *Adv. Mater.* 29 (2017).
- [39] J. Li, B. Shen, Z. Hong, B. Lin, B. Gao, Y. Chen, *Chem. Commun.* 48 (2012) 12017–12019.
- [40] X. She, J. Wu, J. Zhong, H. Xu, Y. Yang, R. Vajtai, J. Lou, Y. Liu, D. Du, H. Li, P.M. Ajayan, *Nano Energy* 27 (2016) 138–146.
- [41] G. Liu, P. Niu, C. Sun, S.C. Smith, Z. Chen, G.Q. Lu, H.-M. Cheng, *J. Am. Chem. Soc.* 132 (2010) 11642–11648.
- [42] H.-B. Fang, Y. Luo, Y.-Z. Zheng, W. Ma, X. Tao, *Ind. Eng. Chem. Res.* 55 (2016) 4506–4514.
- [43] X. Lu, K. Xu, P. Chen, K. Jia, S. Liu, C. Wu, *J. Mater. Chem. A* 2 (2014) 18924–18928.
- [44] W. Xing, C. Li, G. Chen, Z. Han, Y. Zhou, Y. Hu, Q. Meng, *Appl. Catal. B: Environ.* 203 (2017) 65–71.
- [45] S.J. Makowski, P. Kostler, W. Schnick, *Chemistry* 18 (2012) 3248–3257.
- [46] Y. Zhou, L. Zhang, W. Huang, Q. Kong, X. Fan, M. Wang, J. Shi, *Carbon* 99 (2016) 111–117.
- [47] H.-B. Fang, N. Li, Z. Xue, Y. Zhang, Y.-Z. Zheng, X. Tao, *Electrochem. Commun.* 72 (2016) 118–121.
- [48] S. Yang, Y. Gong, J. Zhang, L. Zhan, L. Ma, Z. Fang, R. Vajtai, X. Wang, P.M. Ajayan, *Adv. Mater.* 25 (2013) 2452–2456.
- [49] C.M. Cardona, W. Li, A.E. Kaifer, D. Stockdale, G.C. Bazan, *Adv. Mater.* 23 (2011) 2367–2371.
- [50] S. Zhang, L. Gao, D. Fan, X. Lv, Y. Li, Z. Yan, *Chem. Phys. Lett.* 672 (2017) 26–30.
- [51] J. Zhang, X. Chen, K. Takanabe, K. Maeda, K. Domen, J.D. Epping, X. Fu, M. Antonietti, X. Wang, *Angew. Chem. Int. Ed.* 49 (2010) 441–444.
- [52] Z. Yue, A. Liu, C. Zhang, J. Huang, M. Zhu, Y. Du, P. Yang, *Appl. Catal. B: Environ.* 201 (2017) 202–210.